ADVANCED FUNCTIONAL MATERIALS

Supporting Information

for *Adv. Funct. Mater.*, DOI 10.1002/adfm.202413865

Stabilizing Nickel-Rich Cathodes in Aqueous Process through Nanocellulose as Water Barrier

Ying Wang, Ying Fang, Luyao Huang, Jiwei Wang, Hua Zhou, Guanyi Wang, Qingliu Wu, Guofeng Wang and Hongli Zhu**

Supporting Information

Stabilizing Nickel-Rich Cathodes in Aqueous Process through Nanocellulose as Water Barrier

Ying Wang[1], Ying Fang[2], Luyao Huang[1], Jiwei Wang[1], Hua Zhou[3], Guanyi Wang[4], Qingliu Wu[4], Guofeng Wang[2, *], Hongli Zhu[1, *]

[1] Department of Mechanical and Industrial Engineering, Northeastern University, Boston, MA 02115, USA

[2] Department of Mechanical Engineering and Materials Science, University of Pittsburgh, Pittsburgh, PA, 15260, USA

[3] X-Ray Science Division, Argonne National Laboratory, Lemont, IL, 60439, USA

[4] Department of Chemical and Paper Engineering, Western Michigan University, Kalamazoo, MI, 49008, USA

* Corresponding author: Dr. Hongli Zhu; E-mail: h.zhu@neu.edu, Dr. Guofeng Wang; E-mail: guw8@pitt.edu.

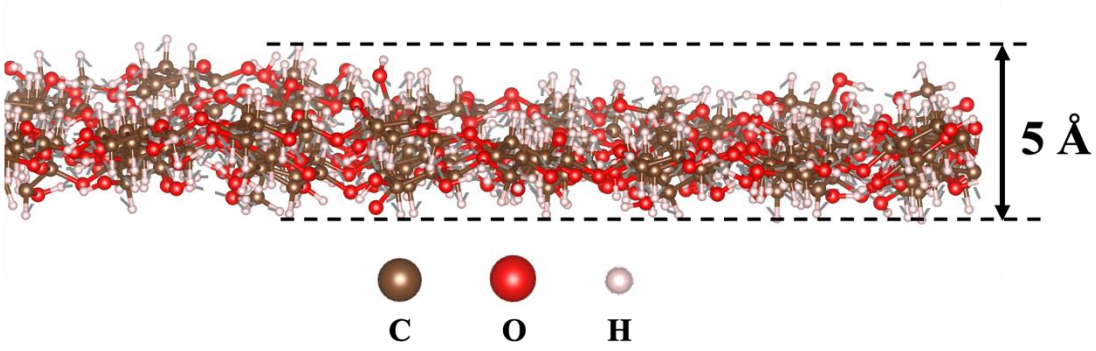

Figure S1. Simulation of a cellulose chain.

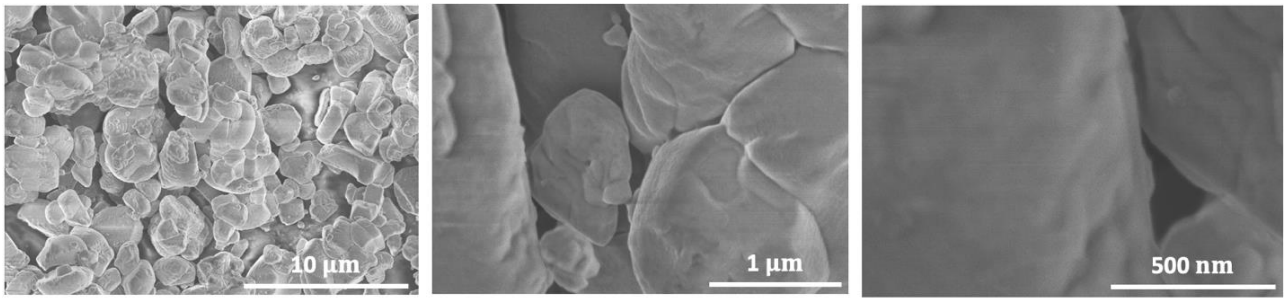

Figure S2. SEM images of single crystalline NMC 811 particles.

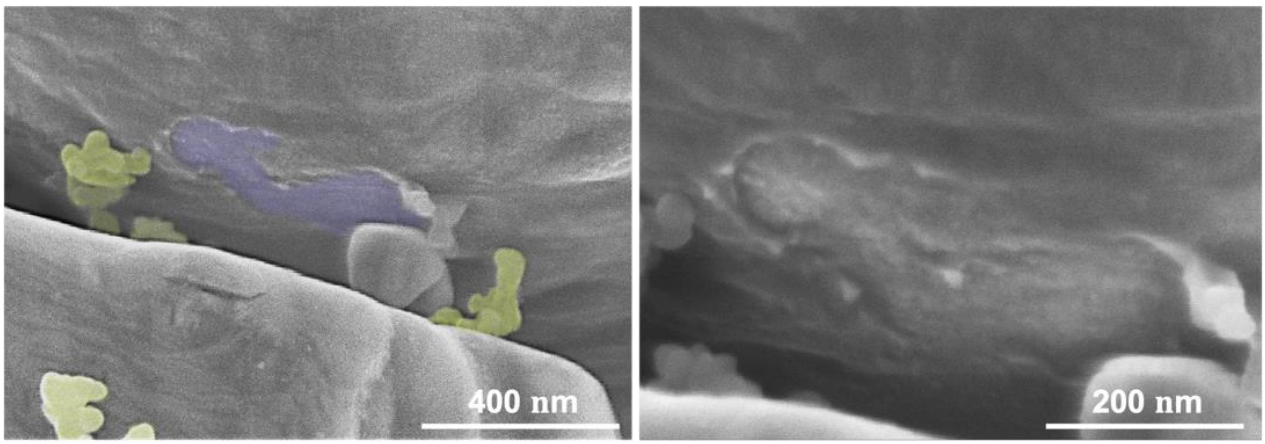

Figure S3. Colored and magnified SEM image of CNC-CNF electrode focusing on NMC particles. Yellow is carbon black, and purple is the exposed area of the NMC particle.

Fluorescence analysis of nanocellulose-coated NMC particles

After the washing process by filtering, **Figures S4A** and **S4B** show no fluorescence signal in NMC particle mixtures combined with CNC-CNF and CNC-CNF filtered water, respectively. These findings indicate that the fluorescent substance exhibits excellent water solubility, making it easy to remove through filtration. Furthermore, it is observed that this fluorescent substance does not undergo any chemical reactions or graft itself to the pure nanocellulose. To address this issue, a small amount of acid was added during the staining procedure. The acid concentration matches that of H^+ CNC-CNF electrodes discussed later in the manuscript. After washing by filtering, the NMC particle combination with H^+ CNC-CNF exhibits strong fluorescence (**Figure S4C**), while no fluorescence is detected in the mixture with H^+ CNC-CNF filtered water (**Figure S4D**). Consequently, the fluorescent substance is effectively grafted to the nanocelluloses, and no additional fluorescence sodium salt dissolves in water. In other words, nanocellulose is the only material that exhibits fluorescence in the characterization.

Figures S4E and **S4F** display highly magnified microscope images and corresponding fluorescent images of a diluted mixture with NMC particles and H^+ CNC-CNF. A significant number of minute individual fluorescent particles possess dimensions ranging from 2 to 4 μm, which aligns with the diameter of as-received NMC particles. Similar results are observed in the confocal laser scanning microscopy images. **Figure S5A** shows numerous clear spherical fluorescent substances, most of which have diameters between 2 to 4 μm. The spherical shape and efficient nanocellulose coating are demonstrated in **Figure S5B** along the Z-axis. Thus, it is proven that nanocelluloses have the ability to autonomously advance and envelop the NMC particles, resulting in effective coverage. However, given the resolution limitation of the optical microscope,[1] these fluorescence images do not quantify the coverage.

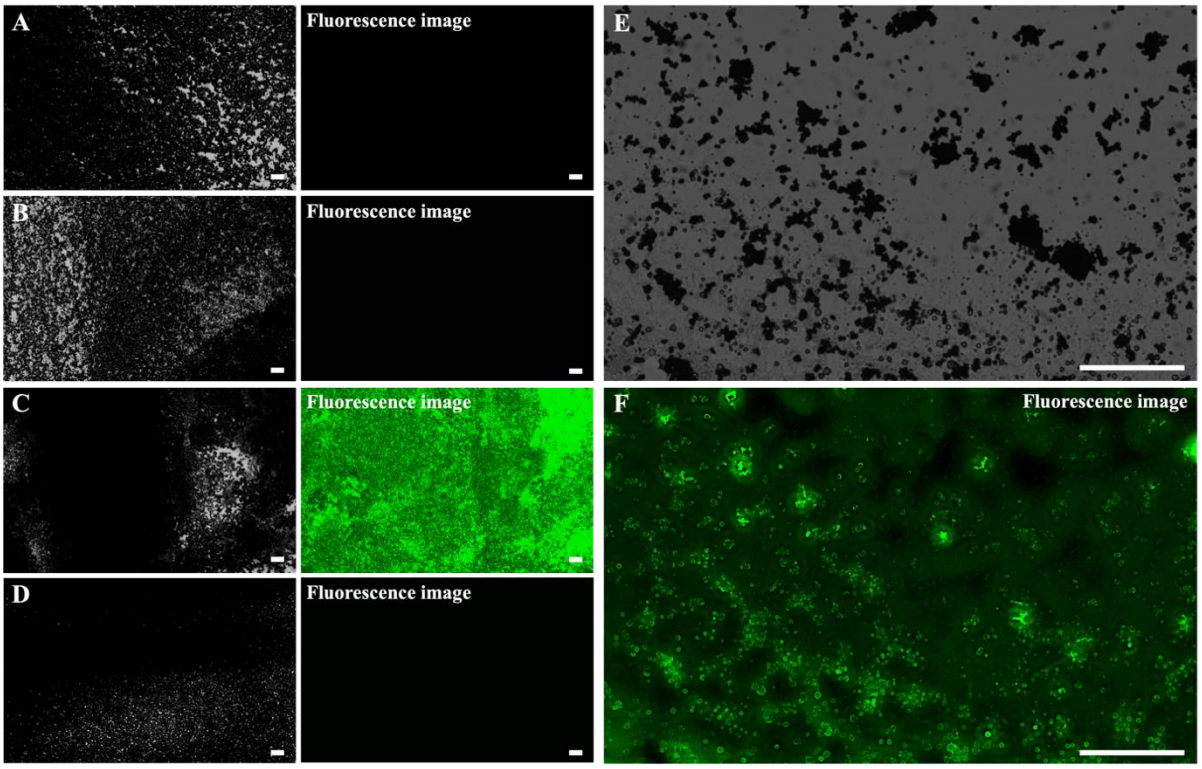

Figure S4. Optical microscope and fluorescence images of NMC particles mixture with (A) CNC-CNF, (B) filtered water of CNC-CNF, (C) H^+ CNC-CNF, and (D) filtered water of H^+ CNC-CNF. (E-F) High magnification optical images of NMC particles and H^+ CNC-CNF mixture. The scale bar is 100 µm for all figures.

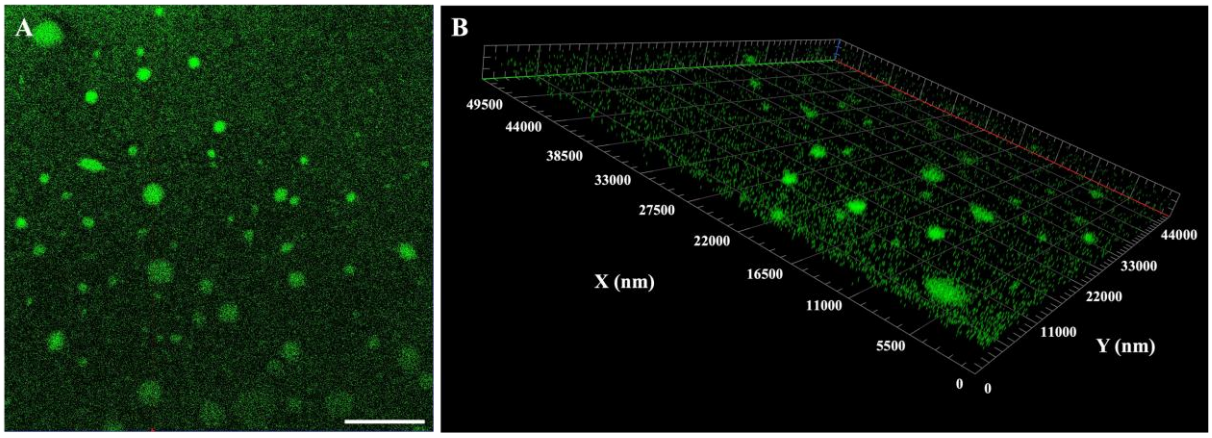

Figure S5. High magnification (A) orthogonal and (B) three-dimensional confocal laser scanning microscopy images of NMC particles and H^+ CNC-CNF mixture. The scale bar is 10 µm.

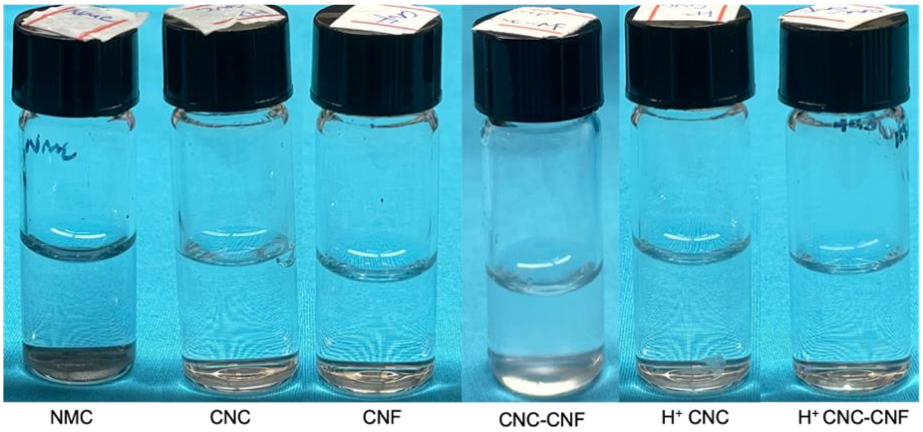

Figure S6. Digital image of 0.05 wt.% NMC particles and cellulose nanomaterials dispersed into water.

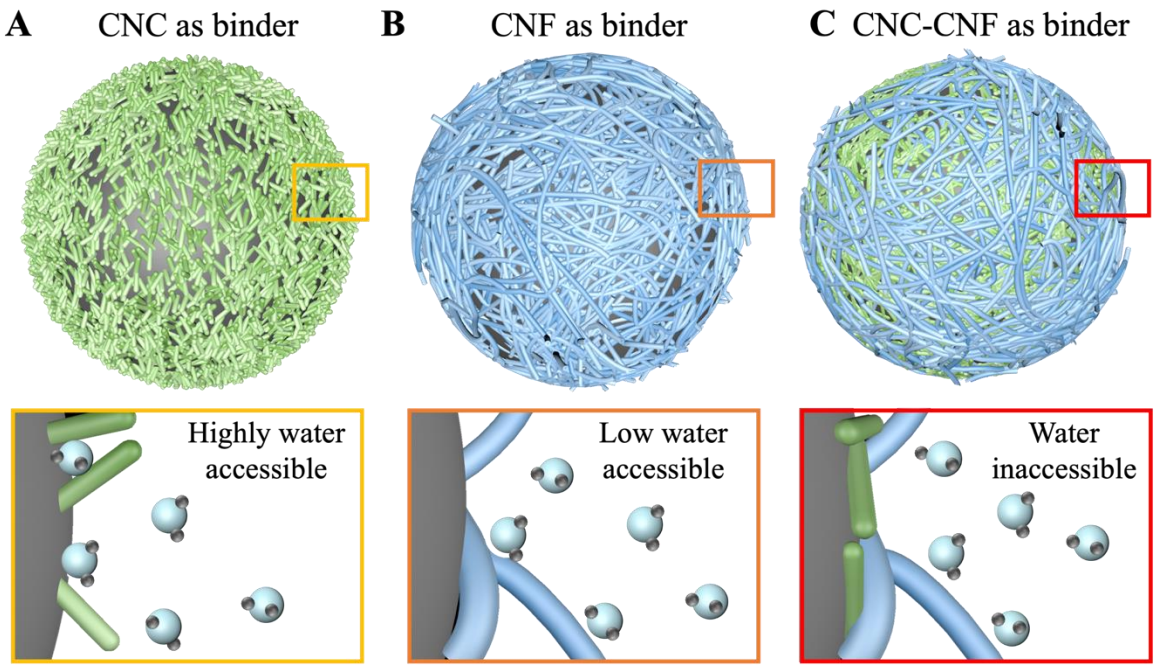

Figure S7. Schematics of coverages composed of (A) CNC, (B) CNF, and (C) CNC-CNF in the aqueous-based system. With the number of nanomaterials, the rod-like CNC lack connection with each other, and it is hard to form a uniform protection film. Different from the CNC, CNF is long enough to be stacked on each other and generate an excellent film to limit water molecules while maintaining some uncovered regions. Superior to using only CNF, the CNC introduction assists in filling the small gaps between the randomly stacked fibers and creating a denser coverage.

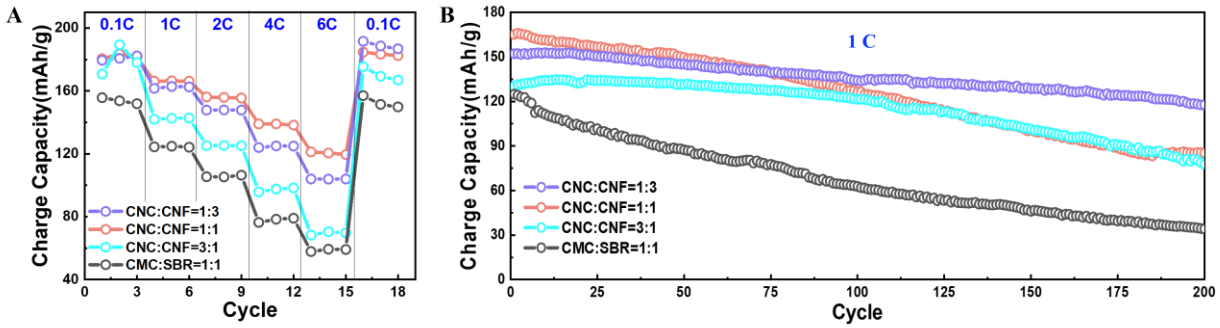

Figure S8. (A) Rate performance and (B) cycling stability of aqueous-based electrodes covered using various CNC and CNF ratios.

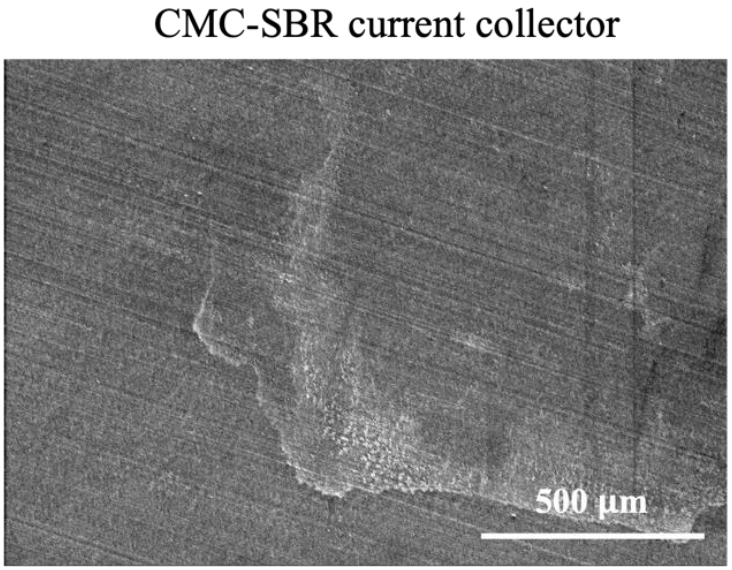

Figure S9. SEM images of the CMC-SBR current collector removed electrode materials.

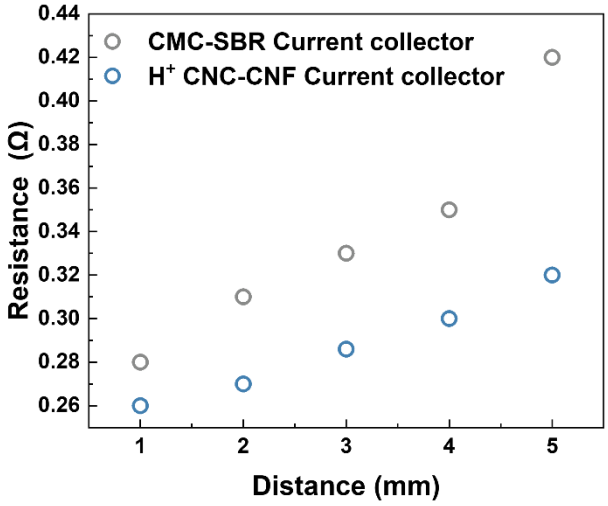

Figure S10. Resistance versus measure distance of current collectors.

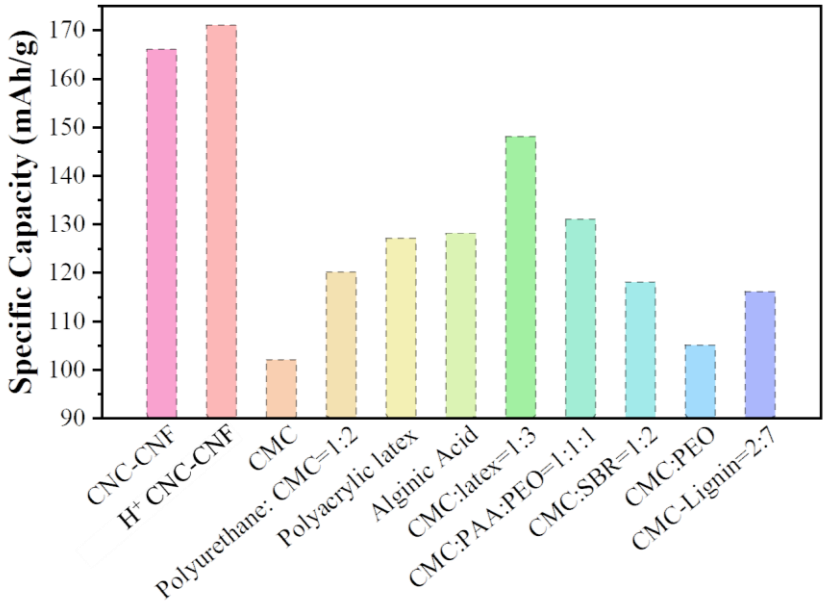

Figure S11. Comparison of aqueous-based NMC electrodes using various binders at a current rate of 1 C.[2]

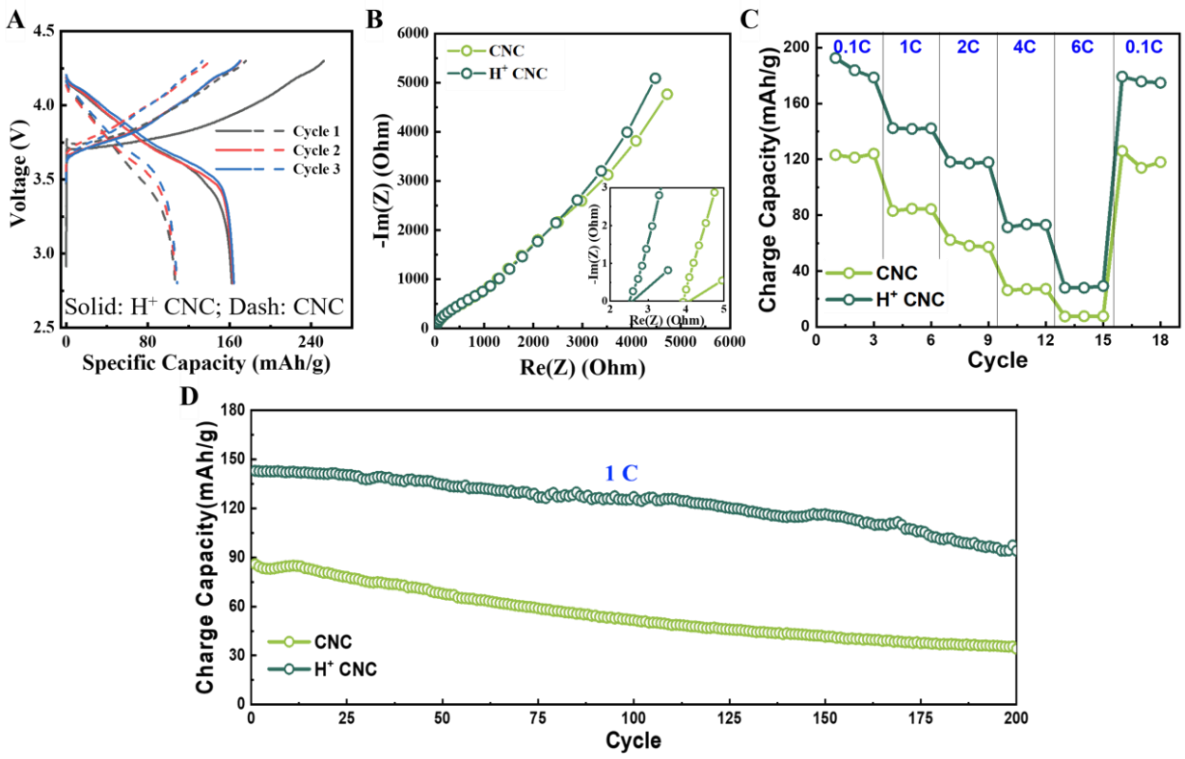

Figure S12. (A) Galvanostatic charge-discharge curves, (B) Nyquist plots, (C) rate performance, and (D) cycling stability of H^+ CNC and CNC electrodes. Obviously, acid modification is necessary for the electrodes using pure CNC as a binder.

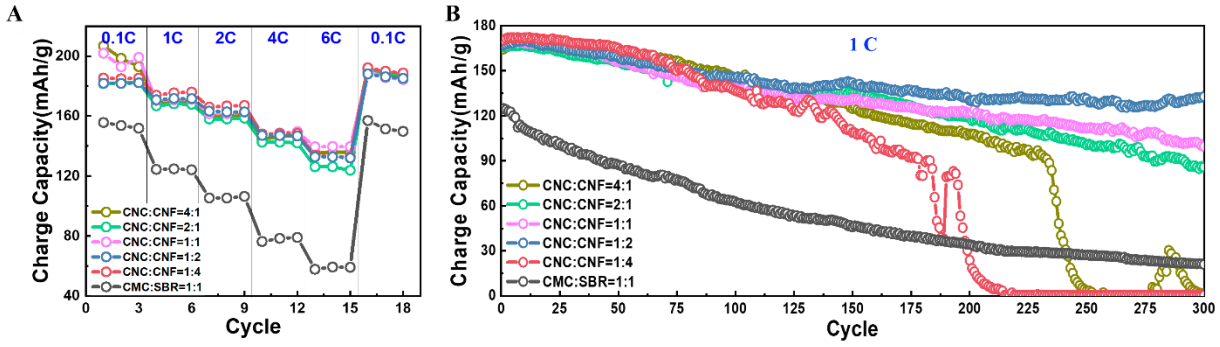

Figure S13. (A) Rate performance and (B) cycling stability of aqueous-based electrodes covered using various H^+ CNC and CNF ratios.

Electrochemical performance comparisons between aqueous-based CNC-CNF electrodes and NMP-based PVDF electrodes

In addition to processing lower charge transfer resistance and improved rate performance comparable to PVDF electrodes (**Figure S14**), the H^+ CNC-CNF electrode performed much better cycling stability than the PVDF electrode, as shown in **Figure S15**. Despite starting with a similar capacity, the PVDF electrode presented signs of decay after 60 cycles and excessive deterioration starting from the 80th cycle. The improved electrochemical stability is attributed to two factors: nanocellulose maintains the stability of the Li metal anode and enhances the connection between the electrode and the current collector.

Previous research reveals that the cycling performance of an NMC half-cell using a Li metal anode is much worse than that of an NMC full-cell using graphite or $Li_4Ti_5O_{12}$ anode.[3] In the half-cell, the electrolyte reacts with the Li metal and undergoes degradation, resulting in the formation of by-products that move through the cell and oxidize on the cathode surface.[4] In this work, the use of thin Li metal with a thickness of 110 μm is a major limitation of the cycling performance of conventional PVDF electrodes. **Figure S16** shows the reduced cycling stability of the NMC half-cell after replacing the Li metal with a thinner thickness of 20 μm. Although the exact reasons need further investigation, adding nanocellulose to the electrolyte can favorably enhance cycling performance. As shown in **Figure S17**, the stability of the NMC half-cell with CNC-included electrolyte was stable for 150 cycles, while the capacity of the control sample started to decay at 60 cycles and dropped to 0 mAh/g at around 100 cycles. After replacing Li metal and refilled electrolyte, the capacity is recovered. Several publications reported that cellulose derivatives can modify the interface to stabilize the Li metal anode.[5] In addition to stabilizing the Li metal anode, H^+ CNC-CNF possesses improved binding ability. **Figure S18** displays the

disassembled coin cell after the cycling test. The H^+ CNC-CNF electrode remains tightly connected to the current collector. In contrast, the PVDF electrode and its current collector delaminate, and the PVDF electrode sticks to the separator. The high adhesion strength results from the heightened hydrogen bonding between the –COOH groups and the –OH groups on the surface of NMC electrodes and the current collector.[6]

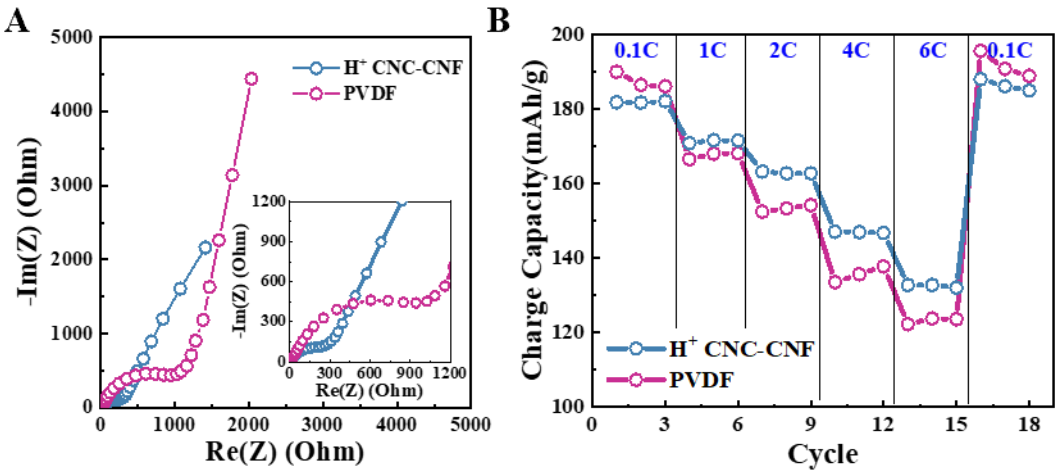

Figure S14. (A) Nyquist plots and (B) rate performance of the aqueous-processed H^+ CNC-CNF electrode and PVDF electrode. Thin Li metal with a thickness of 110 µm was applied.

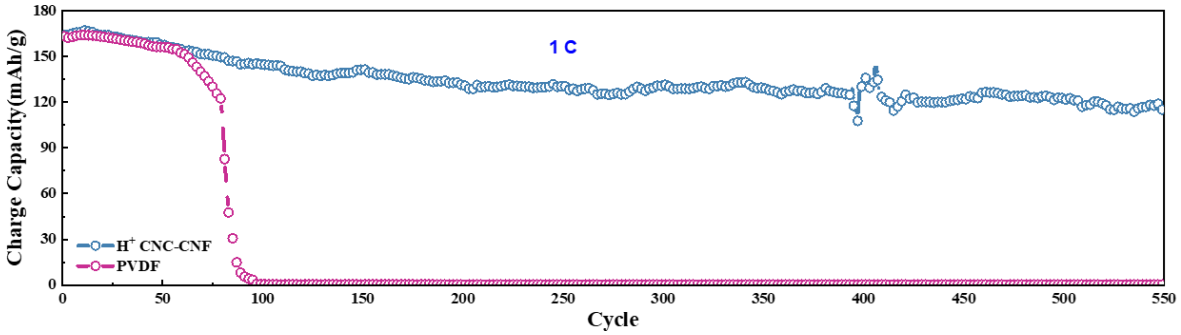

Figure S15. Cycling stability of the aqueous-based H^+ CNC-CNF electrode and NMP-based PVDF electrode. Thin Li metal with a thickness of 110 µm was applied.

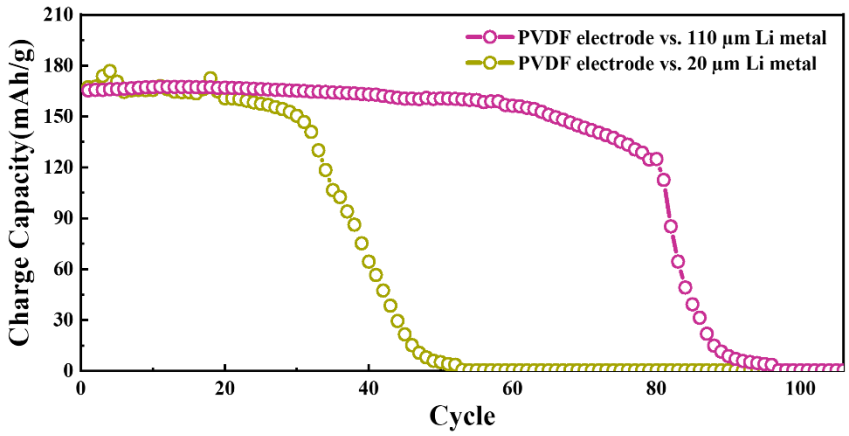

Figure S16. Cycling stability of the NMP-based PVDF electrodes with Li metal anode in 20 and 110 µm thickness.

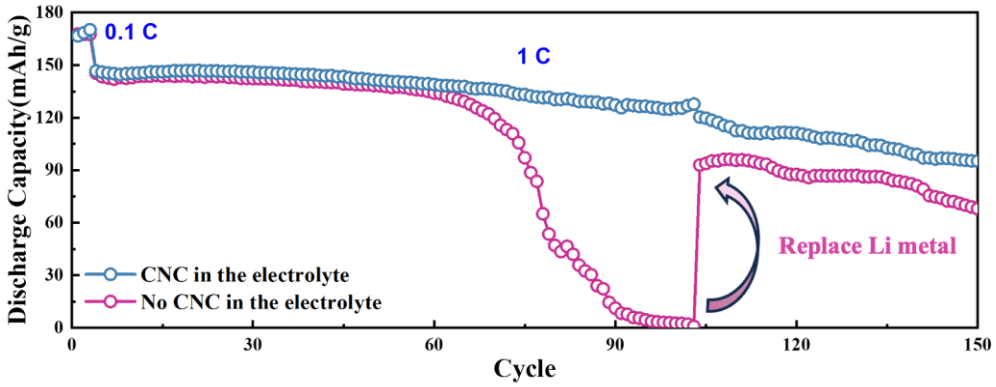

Figure S17. Cycling stability of the PVDF electrode using electrolyte with and without nanocellulose. Thin Li metal with a thickness of 110 µm was applied.

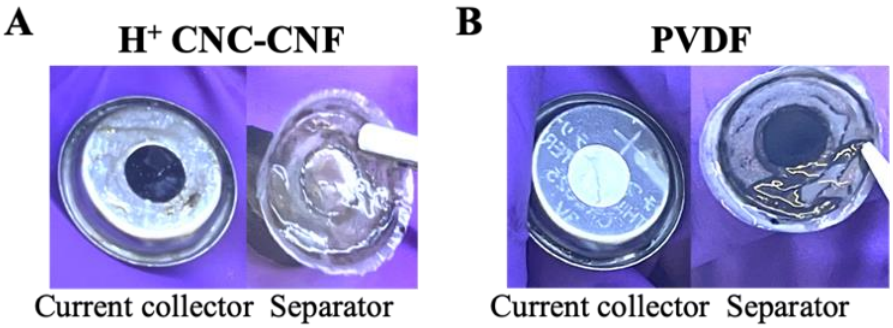

Figure S18. Digital images of disassembled H^+ CNC-CNF and PVDF electrodes after cycling test.

The ability to use screen printing for manufacturing electrodes.

Profiting from the excellent electrochemical performances of nanocelluloses-protected NMC electrodes during water processing, their commercialization can be further realized. Furthermore, the H^+ CNC-CNF electrode slurry has exhibited adequate engineering properties for architecture customization. Since the unique structure of CNC and CNF prevents their mixture from forming a highly twisted network for dragging the particles, the slurry is readily squeezed through the tiny gaps in the screen to render tailored patterns with the electrodes (**Figure S19**).[7] SEM images of the screen printed electrode elucidate the clear pores (**Figure S20**), indicating that it has the potential to enable the realization of specialized functionalities by screen printing various structures.

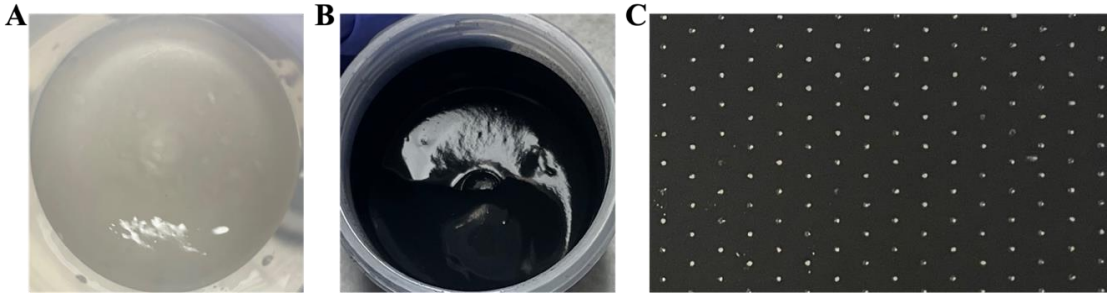

Figure S19. Digital images of (A) H^+ CNC-CNF binder, (B) NMC electrode slurry with H^+ CNC-CNF binder, and (C) a screen-printed electrode on the Al current collector.

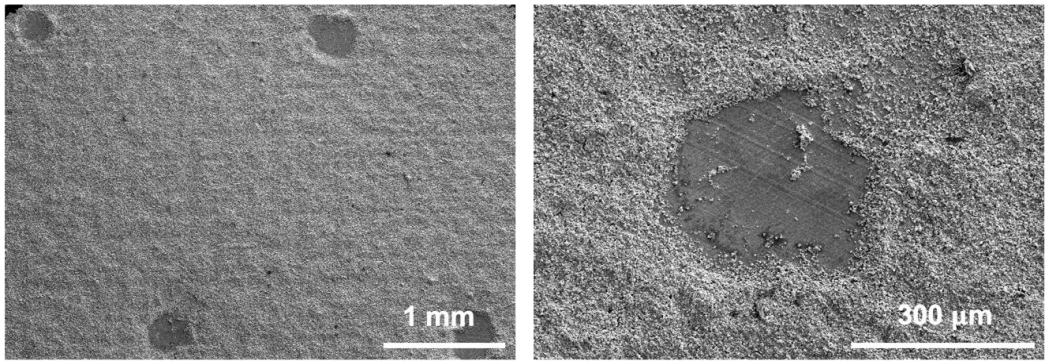

Figure S20. SEM images of screen-printed electrodes with some designed pores.

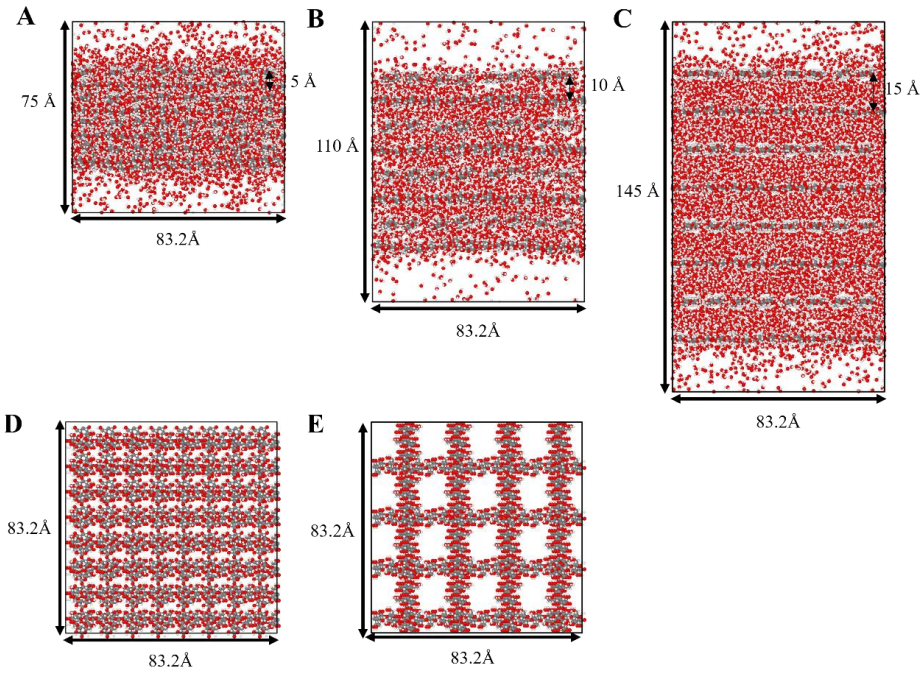

Figure S21. Snapshots of water-cellulose structures from NVT MD simulations with polymer chains separated by 5 Å within each layer and various interlayer spacings: (A) 5 Å, (B) 10 Å, and (C) 15 Å. Top views of porous structures with polymer chains within each layer separated by (D) 5 Å, and (E) 15 Å.

Table S1. Calculated deposit concentration of water-based electrodes through titration method

	CMC-SBR	CNC-CNF	H^+ CNC-CNF
Li_2CO_3 (wt.%)	4.82	1.74	1.21
LiOH (wt.%)	-	-	-

* The concentration of LiOH is calculated to be close to 0 wt.%, which may be due to the exposure to the CO_2 atmosphere during electrode slurries fabrication and drying, which causes all of the LiOH produced to be converted to Li_2CO_3.

Table S2. Calculated adsorption energies of -R-COO, -HSO_3, H_2O, and co-adsorbed -R-COO with H_2O on NMC surface.

	-R-COO	-HSO_3	H_2O	-R-COO +H_2O
Adsorption Energy (eV)	0.16	0.46	0.24	0.42

Calculation results of Li surface segregation energies

In **Table S3**, we presented the DFT calculated Li surface segregation energies in the NMC electrodes with the surface adsorbates of interest. It notes that negative Li surface segregation energy indicates that Li would prefer to migrate to the surface and bind to the adsorbates (i.e., H_2O molecule), whereas positive Li surface segregation energy indicates that Li would prefer to staying inside the electrode materials and not binding to the surface adsorbates (for example, -R-COO). Moreover, our DFT calculations show that the Li surface segregation energy is positive (0.51 eV) in the NMC electrode without any surface adsorbates. During the charge and discharge of batteries, Li ions would migrate under an electrical field through the electrode materials. Since surface adsorbates -R-COO and -HSO_3 will not bind these migrating Li ions, they are not expected to affect the diffusivity of Li ions. We have updated **Table S3** by including the segregation energy without any adsorbate and the newest segregation energies of H_2O and -R-COO.

Table S3. Calculated Li surface segregation energies in nickel-rich $LiNi_{0.8}Co_{0.1}Mn_{0.2}O_2$ (NMC) electrode with various kinds of surface adsorbates.

	Without Adsorbate*	H_2O	-R-COO	$-HSO_3$
Li Segregation Energy (eV)	0.51	-0.89	0.65	0.09

* Bare NMC particles without H_2O, -R-COO, or $-HSO_3$.

Reference

[1] Stelzer, *J. Microsc.* **1998**, 189, 15.

[2] a) I. Doberdò, N. Löffler, N. Laszczynski, D. Cericola, N. Penazzi, S. Bodoardo, G.-T. Kim, S. Passerini, *J. Power Sources* **2014**, 248, 1000; b) N. Loeffler, T. Kopel, G.-T. Kim, S. Passerini, *J. Electrochem. Soc.* **2015**, 162, A2692; c) H. Zhong, M. Sun, Y. Li, J. He, J. Yang, L. Zhang, *J. Solid State Electrochem.* **2016**, 20, 1; d) K. Soeda, M. Yamagata, M. Ishikawa, *ECS Trans.* **2015**, 64, 13; e) M. Bichon, D. Sotta, N. Dupré, E. De Vito, A. Boulineau, W. Porcher, B. Lestriez, *ACS Appl. Mater. Interfaces* **2019**, 11, 18331; f) L. Ibing, T. Gallasch, P. Schneider, P. Niehoff, A. Hintennach, M. Winter, F. M. Schappacher, *J. Power Sources* **2019**, 423, 183; g) R. Demiryürek, N. Gürbüz, G. Hatipoglu, M. Er, H. Malkoc, O. Guleryuz, G. Uyar, D. Uzun, M. N. Ateş, *Int. J. Energy Res.* **2021**, 45, 21182; h) S. N. Bryntesen, I. Tolstorebrov, A. M. Svensson, P. Shearing, J. J. Lamb, O. S. Burheim, *Mater. Adv.* **2023**, 4, 523.

[3] M. Bichon, D. Sotta, N. Dupré, E. De Vito, A. Boulineau, W. Porcher, B. Lestriez, *ACS Appl. Mater. Interfaces* **2019**, 11, 18331.

[4] R. C. McNulty, E. Hampson, L. N. Cutler, C. P. Grey, W. M. Dose, L. R. Johnson, *J. Mater. Chem. A* **2023**, 11, 18302.

[5] a) M. Chen, J. Zheng, Y. Liu, O. Sheng, Z. Ju, G. Lu, T. Liu, Y. Wang, J. Nai, Q. Wang, *Adv. Funct. Mater.* **2021**, 31, 2102228; b) S. Li, Y. Huang, C. Luo, W. Ren, J. Yang, X. Li, M. Wang, H. Cao, *Chem. Eng. J.* **2020**, 399, 125687; c) Y. Luo, T. Li, H. Zhang, W. Liu, X. Zhang, J. Yan, H. Zhang, X. Li, *Angew. Chem. Int. Ed.* **2021**, 60, 11718; d) K. Kim, P. J. Kim, R. A. Chowdhury, R. Kantharaj, A. Candadai, A. Marconnet, V. G. Pol, J. P. Youngblood, *Chem. Eng. J.* **2021**, 417, 128128.

[6] a) J. Lee, K. Lee, T. Lee, H. Kim, K. Kim, W. Cho, A. Coskun, K. Char, J. W. Choi, *Adv. Mater.* **2020**, 32, 2001702; b) D. Jeong, D. S. Kwon, H. J. Kim, J. Shim, *Adv. Energy Mater.* **2023**, 2302845.

[7] a) Y. Wang, J. He, D. Cao, E. Cakmak, X. Zhao, Q. Wu, Y. Zhao, H. Ren, X. Sun, Y. Li, *Energy Storage Mater.* **2023**, 55, 42; b) Y. Wang, Y. Zhang, D. Cao, T. Ji, H. Ren, G. Wang, Q. Wu, H. Zhu, *Small Methods* **2023**, 7, 2201344.